A PENDULUM BASED FREQUENCY-UP CONVERSION MECHANISM FOR VIBRATIONAL ENERGY HARVESTING IN LOW-SPEED ROTARY STRUCTURES

Weijie Xian
Department of Mechanical Engineering, University of Maryland Baltimore County.
Department of Mechanical Engineering, 1000 Hilltop Rd, Baltimore, MD 21250.
xiaw1@umbc.edu

Soobum Lee
Department of Mechanical Engineering, University of Maryland Baltimore County.
Department of Mechanical Engineering, 1000 Hilltop Rd, Baltimore, MD 21250.
sblee@umbc.edu

ABSTRACT

Motivated to run a self-powering monitoring sensor on a wind turbine blade, this paper proposes a pendulum based frequency up converter that effectively captures a low-speed mechanical rotation into high-frequency vibration of a piezoelectric cantilever beam. A system of governing equations for the proposed concept is developed to describe the motion of the pendulum, the vibration of the beam, and the voltage output of the harvester. Design optimization is performed to improve the power generation performance, and the simulation results are verified experimentally. We demonstrate the improved power density from the proposed concept compared to the disk driven frequency up converters.

1. Introduction

For the past decade, energy harvesting techniques have gathered more attention, mainly due to the rapid advance in technology of low-power wireless sensor networks. Such networks have an enormous potential to be utilized for many practical monitoring tasks with extremely low power consumption (Knight and Davidson, 2008, pp. 8037-8066; Yan et al., 2020). Batteries are the power sources for most of the sensor nodes, but they have unsolved issues such as power leakage, chemical leakage, and labor cost for battery replacement (Shaikh and Zeadally, 2016, pp. 1041-1054). These problems can be solved by using energy harvesting technology, which has been advanced to accommodate easy implementation, high efficiency, low cost, and high durability to be a more practical power solution to the sensor networks (Yan et al., 2020).

There are several techniques for harvesting environmental energy: solar, heat, wind, radio frequency, and vibrations. A piezoelectric energy harvester (PEH) has been studied as a method to convert vibrational energy into electrical energy. PEH benefited from its simple structure, ease of implementation, and high-power output compared to various harvesting techniques (Liu, 2018; Xing et al., 2009; Erturk and Inman, 2011, pp. 1-71; Kim et al., 2011, pp. 1129-1141). Recently, there has been a variety of applications of piezoelectric harvesters by harvesting energy from animals/human bodies, machinery, vehicles, bridges, road, water flow, and wind (Yang et al., 2018, pp. 642-697; Zhang et al., 2017, pp. 123-129; Yang et al., 2014; Xu et al., 2017, pp. 388-395; Liu et al., 2020, pp. 1459-1479, Choudhry, Khalid and Lee, pp. 3346-3357). While the piezoelectric harvester can be used anywhere with vibrations, the hardest task that most researchers face is to improve its power generation level by matching the ambient frequency to the natural frequency of the PEH.

In most cases, a piezoelectric harvester system can only perform efficiently at its resonant frequency (Ong, Huang, and Chou, 2019, pp. 779-793). Zhang et al. (2017, pp. 123-129) found that the piezoelectric beam generates reliable power output when it is excited at a frequency between 80-110 Hz. This makes it hard to harvest a low speed vibration from a large rotary structure like a wind turbine blade that has a rotational frequency of less than 1 Hz or 60 RPM, and the piezoelectric actuator will not be able to generate a practical amount of power if installed directly on these large rotary structures. Numerous studies about manipulating the frequency of either excitation structures or piezoelectric actuators have been conducted. Wu et al. (2014, pp. 1875-1889) proposed a 2 DOF nonlinear piezoelectric energy harvester that significantly broadens operating bandwidth. The design consists of two cantilever beams, which create two resonance frequencies, and two magnets, which add nonlinearity characteristics to the design to remove anti-resonance frequency. A similar design with a dual-cantilever structure and magnet-induced piezoelectric harvester was carried out by Su et al. (2014, pp. 430-442). Erturk et al. (2019, pp. 529-544) introduced an L-shaped beam consisting of three piezoelectric beams and two masses to achieve broader bandwidth than a simple cantilever beam. Hu. et al. (2006, pp. 649-659) have studied a spiral-shaped bimorph piezoelectric harvester. It was found that spiral-shaped structure operates at a lower frequency compared to beam structure. The broadband harvester concepts could improve the harvester performance even when the frequency input is varied, but they still have limited performance in utilizing low-frequency vibrations.

There are several studies designing harvester devices with frequency up-conversion techniques that convert low frequency from the rotary structure to higher frequency, to match the frequency of the piezoelectric actuator. Fu and Yeatman (2019, pp. 229-244) studied a piezoelectric harvester using a bi-stability design. This design utilized two sets of magnets to excite the

piezoelectric beam; it could vibrate the piezoelectric beam at resonance frequency with a driving frequency of 5 Hz. Wang et al. (2019, pp. 2371-2397) proposed a design of a tri-stable piezoelectric harvester using two external magnets and significantly enhanced the power performance compared to a bi-stable design. Pozzi and Zhu (2012) designed a rotational harvester which used the plectrum effect to achieve frequency-up conversion. However, Pozzi and Zhu's design created significant vibrational interference in the structure. Fang et al. (2019) proposed a music-box-like plucking energy harvester to solve the issue. Park et al. (2012) even performed a shape optimization study for the plucking harvester.

This paper presents a new frequency up converter, motivated to devise a self-powering monitoring sensor node for wind turbine blades. Wind energy is the third-largest power source in the U.S, and the number of wind turbines is increasing dramatically in the recent decade (Wiser and Bolinger, 2001; Konstantinidis and Botsaris, 2016). It is significant to implement a self-powering sensor network to monitor the health of wind turbine blades. A self-powering sensor that harvests ambient energy could help to reduce operational and manufacturing costs compared to conventional sensors with wires. This benefit includes simplifying the wire installation process and reducing the cost of battery replacement. The frequency up converter design introduced in this paper utilizes gravitational and magnetic force. Detailed conceptual designs and dynamic equations are derived using Lagrange's method. The performance of this concept is optimized to generate practical power output suited for rotary objects in low frequency, such as wind turbine blades less than 1 Hz rotational speed. The design results are verified experimentally to demonstrate the improved power density compared to the disk driven frequency up converters (Nezami and Lee, 2020). It is noted that the proposed frequency up

converter is not limitedly used for a wind turbine blade but able to be applied to any slow rotary systems.

The overall organization of this paper is as follows: Section 2 demonstrates the conceptual designs and mathematical model derivations of the pendulum and disk driven harvesters. Section 3 shows the simulation results and design optimizations, and the results are verified experimentally in Section 4. This paper is then concluded in Section 5.

2.   Conceptual Designs and Mathematical Model Derivation of Harvester Dynamics

This paper investigates a pendulum based frequency-up converter for cantilevered piezoelectric energy harvesters that will efficiently utilize low rotational motion of wind turbine blades. We also demonstrate a disk driven converter for comparison purpose.

2.1. Pendulum based frequency up converter
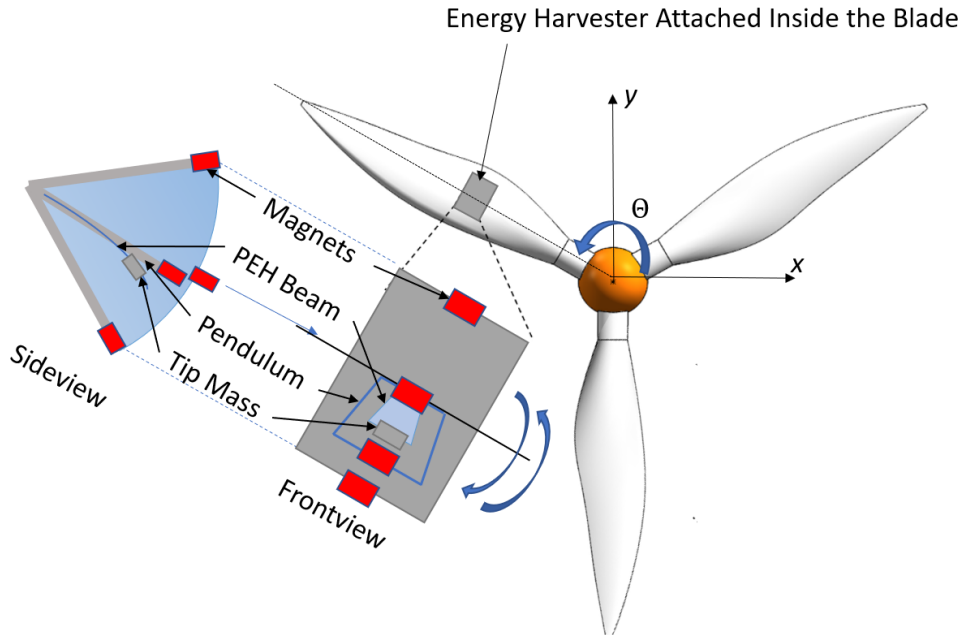
Figure (2.1) Configuration of the proposed harvester on a wind turbine blade

Figure (2.1) shows the configuration of the newly proposed pendulum based frequency up converter and the harvester on a wind turbine, while Figure (2.2) shows its schematic model. It mainly consists of a pendulum swinging in a circular sector. The swinging of the pendulum is controlled by three fixed magnets, one in the middle (m_M) and the other two (m_T and m_B) on the outer bounds of the circular sector. The fourth magnet is attached on the tip of moving pendulum (m_P). The intermediate magnet (m_M) holds the pendulum until it has enough downward force by gravity. Holding the pendulum is important because it enables a sudden downward motion when the gravitational force becomes larger. The piezoelectric beam is mounted on the pendulum, so that voltage is induced when the pendulum swings.
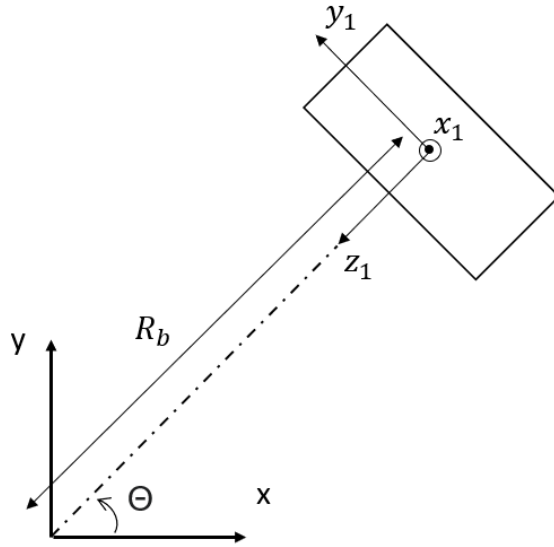
(a) With Respect to Global
Coordinate (x, y)
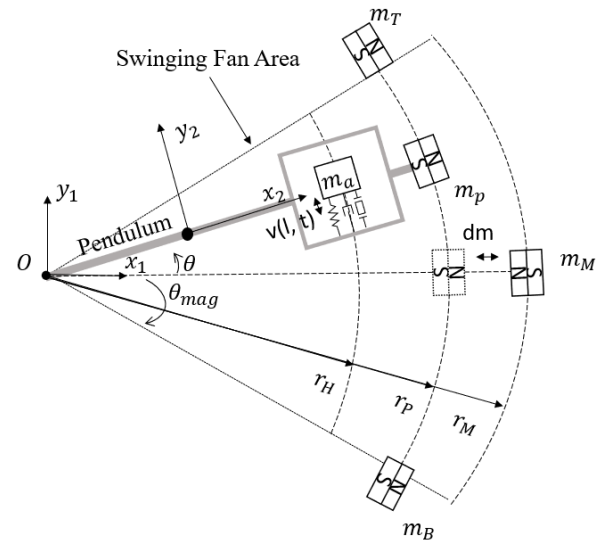
(a) With Respect to Local
Coordinate (x_1, y_1)

Figure (2.2) Schematic model of the harvester setup

The equation of motion is derived to demonstrate the energy harvesting performance as follows. There are 3 coordinates: a global coordinate system (X, Y, Z) at the center of the rotation of the blade, 2 local coordinate systems, (x_1, y_1, z_1) at the pivot point of the pendulum, and (x_2, y_2, z_2)

at the root of the cantilevered PEH beam. Θ describes the blade orientation with respect to global coordinates (X, Y, Z), θ is the angular position of the pendulum with respect to the local coordinates (x_1, y_1, z_1), and v is the local position of the tip mass of the harvester.

The following assumptions are made to simplify the modeling process of the proposed harvesters in this paper as follows:

- The cantilevered beam is assumed to be an Euler Bernoulli beam with a uniform cross-section, linear stiffness, and small deflection.

- The damping ratios of the pendulum swing and the beam deflection are assumed to be constant.

- Magnetic repelling force is assumed to be a function of the distance between two magnets and the effect of magnet rotation is neglected.

- Only the first mode shape function is considered for the beam vibration.

Table (2.1) shows the design variables used during the mathematical modeling process.

Table (2.1) Variables used in the mathematical model

Symbol	Description
R_b	Center of the harvester to origin of the global coordinate
r_P	Length of the pendulum
r_H	Distance from the local coordinate origin to the harvester tip mass
r_M	Distance from the local coordinate origin to the intermediate magnet
l	Length of the PZT harvester
Θ	Angular position of the harvester in global coordinate
θ	Angular position of the pendulum in local coordinate
θ_{mag}	Angular displacement of the outer magnet to the center of the pendulum swinging area

The location of the pendulum tip in the global coordinate is:

$$\begin{cases} x_p = R_b\cos\Theta - r_p\sin\theta\sin\Theta \\ y_p = R_b\sin\Theta + r_p\sin\theta\cos\Theta \\ \quad z_p = r_p\cos\theta \end{cases} \tag{2.1}$$

The location of the PEH beam tip mass:

$$\begin{cases} x_t = R_b\cos\Theta - r_H\sin\theta\sin\Theta - v(l,t)\cos\theta\sin\Theta \\ y_t = R_b\sin\Theta + r_H\sin\theta\cos\Theta + v(l,t)\cos\theta\cos\Theta \\ \quad z_{tf} = r_H\cos\theta - v(l,t)\sin\theta \end{cases} \tag{2.2}$$

$v(l)$ describes the vibration of the PEH with respect to the local coordinate system (x_2, y_2, z_2), and

l indicates the PEH beam length. The reduced vibration mode of the cantilever beam, $v(x_2)$ in the

discretized modal coordinate can be formulated as:

$$v(x_2, t) = \phi(x_2)q(t) \tag{2.3}$$

$q(t)$ is the normal coordinate and $\phi(x_2)$ is the first mode shape function of the cantilevered beam

as:

$$\phi_n(x_2) = \cosh(\beta x_2) - \cos(\beta x_2) - \sigma(\sinh\beta x_2 - \sin\beta x_2)$$

$$\begin{cases} \beta \times l = 1.87510407 \\ \sigma = 0.7341 \end{cases} \tag{2.4}$$

Similar to equation (2.2), the location of any part of the cantilevered beam is written as:

$$\begin{cases} x_s = R_b\cos\Theta - (r_H - l + x_2)\sin\theta\sin\Theta - v(x2,t)\cos\theta\sin\Theta \\ y_s = R_b\sin\Theta + (r_H - l + x_2)\sin\theta\cos\Theta + v(x2,t)\cos\theta\cos\Theta \\ \quad z_s = (r_H - l + x_2)\cos\theta - v(x2,t)\sin\theta \end{cases} \tag{2.5}$$

In this study, the energy method and Lagrange's equation are used to derive the equation of

motions of the system. Using the energy method significantly simplifies the derivation of the

governing differential equations of motion (Palazzolo, 2016). This method provides a tool to

consider the distributed mass of the flexible PEH beam and magnetic potential energy in the analytical model.

The kinetic energy of the design concept can be written as:

$$T = \frac{1}{2}(I_p + I_b) * \dot{\theta}^2 + \frac{1}{2}m_a(\dot{x}_t^2 + \dot{y}_t^2 + \dot{z}_t^2) + \frac{1}{2}m_s \int_0^l (\dot{x}_s^2 + \dot{y}_s^2 + \dot{z}_s^2)dx_2 \qquad (2.6)$$

where $I_P = m_P r_p^2$, $I_b = \frac{1}{2}m_c r_p^2$, indicated as moment of inertia of pendulum tip, pendulum, respectively; m_P is the mass of magnets(all magnets are identical in the design); m_a, m_c, m_s are mass attached to the PEH, mass of the pendulum, and mass per length (kg/m) of the PEH beam, respectively.

The total potential energy of the energy harvester can be expressed as:

$$U_{total} = U_p + U_t + U_s + U_e + U_{mp} + U_v \qquad (2.7)$$

where U_p, U_t, and U_s are the gravitational energy of the pendulum, pendulum tip, harvester tip mass, and harvester, respectively. U_e is the elastic potential energy of the PEH, U_{mp} is the magnetic potential energy between magnets, and U_v is the electrical potential energy of the PEH.

The magnetic potential energy can be calculated from the work-energy theorem (Equation (2.8)). The magnetic force between the two magnets is extracted from experimental data that will be shown in Appendix. Using a two-term exponential function to interpolate, the force data can be represented as Equation (2.9).

$$U_{mp} = -\int_{r_1}^{r_2} F(r)\partial r \qquad (2.8)$$

$$F(x) = ae^{bx} + ce^{dx} \qquad (2.9)$$

Substituting Equation (2.9) in Equation (2.8), the magnetic potential can be written as:

$$U_{mp} = -\frac{a}{b}e^{b \times l_T} - \frac{c}{d}e^{d \times l_T} - \frac{a}{b}e^{b \times l_B} - \frac{c}{d}e^{d \times l_B} - \frac{a}{b}e^{b \times l_M} - \frac{c}{d}e^{d \times l_M} \qquad (2.10)$$

where $l_T, l_B,$ and l_M are magnetic distances between m_P and three other magnets, written as:

$$l_T = 2r_P \sin\left(\frac{1}{2}\left(\theta_{mag} - \theta(t)\right)\right) \tag{2.11}$$

$$l_B = 2r_P \sin\left(\frac{1}{2}\left(\theta_{mag} + \theta(t)\right)\right) \tag{2.12}$$

$$l_M = \sqrt{\left(\left(r_p\cos\theta(t) - r_M\right)^2 + \left(r_p\sin\theta(t)\right)^2\right)} \tag{2.13}$$

The strain energy of the PZT layers is defined as [18]:

$$U_{vp} = -\frac{1}{2}\int_0^{lp} \upsilon_p V_1(t)\frac{\partial^2 v_1(x_2)}{\partial x_2{}^2}dx_2 + \frac{1}{2}C_p V_1{}^2(t) - \frac{1}{2}\int_0^{lp} \upsilon_p V_2(t)\frac{\partial^2 v_2(x_3)}{\partial x_3{}^2}dx_3 + \frac{1}{2}C_p V_2{}^2(t) \tag{2.14}$$

where $V(t)$ is the voltage across the electrodes on the PEH domain, υ_p is the electromechanical coupling term (Erturk and Inman, 2018, p.15), and C_p is the capacitance of PZT defined as:

$$\upsilon_p = \frac{e_{31}b_p}{h_p}\left[\left(h_p + \frac{h_s}{2}\right)^2 - \frac{h_s{}^2}{4}\right] \times H\left(l_p - x\right) \tag{2.15}$$

$$C_p = \varepsilon_{33}\frac{b_p l_p}{h_p} \tag{2.16}$$

where $e_{33} = d_{31}E_p$ and $\varepsilon_{33} = d_{31}/g_{31}$.

The potential energy of the energy harvester can be formulated as:

$$U = m_P g y_p + m_a g y_t + g m_s \int_0^l y_s dx_2 + \frac{1}{2}\int_0^l EI v''^2 dx_2 - \frac{1}{2}\int_0^l \upsilon_p V(t)v''^2\, dx_2 + \frac{1}{2}C_p V^2(t) -$$

$$\frac{a}{b}e^{bl_M} - \frac{c}{d}e^{dl_M} - \frac{a}{b}e^{bl_T} - \frac{c}{d}e^{dl_T} - \frac{a}{b}e^{bl_B} - \frac{c}{d}e^{dl_B} \tag{2.17}$$

Using the electromechanical Lagrange's equation based on the extended Hamilton's principle (Yang et al., 2018, pp. 642-697), a system of three equations of motion for the EH is derived as:

$$\frac{d}{dt}\left(\frac{\partial T}{\partial \dot{q}_i}\right) - \frac{\partial T}{\partial q_i} + \frac{\partial U}{\partial q_i} = \frac{\delta W}{\delta q_i} \qquad (2.18)$$

$$\frac{d}{dt}\left(\frac{\partial T}{\partial \dot{\theta}}\right) - \frac{\partial T}{\partial \theta} + \frac{\partial U}{\partial \theta} = \frac{\delta W}{\delta \theta} \qquad (2.19)$$

Substituting equations (2.6), and (2.17) into equations (2.18), and (2.19), and taking

corresponding derivatives will result in the following equations:

$$c_1 \dot{q}(t) + \left(m_a r_H^2 + m_s r_s^2 - r_P^2(0.5 m_c + m_P)\right)\ddot{\theta}(t)$$

$$+ \left(m_a \phi(l) r_H + m_s \int_0^l \phi(y_1) dy_1 \, r_s + q(t)\right)\ddot{q}(t)$$

$$+ \left(m_a \phi(l) + m_s \int_0^l \phi(y_1) dy_1\right) g \cos(\theta(t)) \cos(\Theta) + \alpha q(t) - \chi V(t)$$

$$- q(t)\left(\dot{\theta}^2(t) + \cos^2(\theta(t)) \dot{\Theta}^2\right)$$

$$-0.5 * \left(m_a \phi(l) r_H + m_s r_s \int_0^l \phi(y_1) dy_1\right) \sin(2\theta(t)) \, \Theta^2 = 0 \qquad (2.20)$$

$$c_2 \dot{\theta}(t) + \left(m_a \phi(l) r_H + m_s \int_0^l \phi(y_1) dy_1 \, r_s\right)\ddot{\theta}(t) + \ddot{q}(t)$$

$$+(l m_s r_H - 0.5 l^2 m_s + m_a r_H + m_P r_P) g \cos(\theta(t)) \cos\Theta - (0.5 m_a r_H^2 + 0.5 m_s r_s^2) \sin(2\theta(t)) \, \Theta^2$$

$$+q(t)\left(2\dot{q}(t)\dot{\theta}(t) + 0.5 q(t) \sin(2\theta(t)) \dot{\Theta}^2\right)$$

$$- \left(m_a \phi(l) + m_s \int_0^l \phi(y_1) dy_1\right) g q(t) \cos\Theta \sin(\theta(t))$$

$$- \left(m_a \phi(l) r_H + m_s r_s \int_0^l \phi(y_1) dy_1\right) q(t) \cos(2\theta(t)) \, \Theta^2$$

$$-\frac{a * exp\left(b\sqrt{r_M^2 + r_P^2 - 2r_M r_P \cos(\theta(t))}\right) + c * exp\left(d\sqrt{r_M^2 + r_P^2 - 2r_M r_P \cos(\theta(t))}\right)}{\sqrt{r_M^2 + r_P^2 - 2r_M r_P \cos(\theta(t))}}$$

$$+r_P \cos\left(\frac{1}{2}\left(\theta_{mag} - \theta(t)\right)\right)\left(ae^{2b*r_P \sin\left(\frac{1}{2}\left(\theta_{mag}-\theta(t)\right)\right)} + ce^{2d*r_P \sin\left(\frac{1}{2}\left(\theta_{mag}-\theta(t)\right)\right)}\right)$$

$$-r_P \cos\left(\frac{1}{2}\left(\theta_{mag} + \theta(t)\right)\right)\left(ae^{2b*r_P \sin\left(\frac{1}{2}\left(\theta_{mag}+\theta(t)\right)\right)} + ce^{2d*r_P \sin\left(\frac{1}{2}\left(\theta_{mag}+\theta(t)\right)\right)}\right) = 0 \quad (2.21)$$

where $\phi(x) = C\phi_n(x)$ and ϕ_n is the normalized shape function presented in Equation (2.4). To meet the orthogonality of the eigenfunctions, C is calculated to satisfy the following equation:

$$\int_0^l m_{sp} \phi^2(x_2)dx_2 + m_t\phi^2(l) = 1 \quad (2.22)$$

The governing electrical equation based on Kirchhoff's law can be described as below:

$$C_p \frac{dv_p(t)}{dt} + \frac{v_p(t)}{2R_l} - i_p = 0 \quad (2.23)$$

where $i_p = -\kappa\frac{dq(t)}{dt}$, and κ is the modeling coupling term $\kappa = e_{31}h_{pc}b\frac{d\phi(x)}{dx}\Big|_{x=l}$, and h_{pc} describes the distance from the piezoelectric material to the neutral axis.

Equations (2.20), (2.21), and (2.23) are the completed ODE equation set.Table (2.1) shows the design variables used during the mathematical modeling process.

Table (2.1) shows the modeling constants of the design concept.

Table (2.1) Modeling parameters for the harvester

Symbol	Description	Value
h_p	Thickness of PZT layer	0.00015 [m]
h_{ps}	Thickness of substrate between two PZT layers	0.00014 [m]
h_s	Thickness of PPA-2011	0.00076 [m]
l_{ma}	Length of magnet	0.0191 [m]
l_p	Length of PZT layer	0.0402 [m]
l_s	Effective length of PPA-2011	0.0465 [m]
m_m	Weight of magnet	0.0115 [kg]
m_s	Mass per length of PPA-2011	0.062738 [kg]
R_b	Distance of harvester center from O	0.6 [m]
w_m	Width of magnet	0.0064 [m]

2.2. Disk driven frequency up converter

This section introduces the modified version of frequency up converter with a rotating disk, to compare the performance with the pendulum based one. This concept is based on the previous studies (Figure (2.3)) done by Nazami and Lee (2020). Similar to the pendulum based converter, the disk orientation is toward the ground due to gravity while the cantilevered harvester follows the blade orientation. However, the disk rotation is not limited to a circular sector.

We devise two kinds of disk driven harvesters by placing cantilevered piezoelectric harvesters at different positions: (1) laterally next to the disk (Figure (2.4)); and (2) below the circular disk area (Figure (2.5)). The cantilevered harvester geometry is shown in Figure (2.4(a)) and Figure (2.5(b)) and its symbolic representation is shown in Figure (2.4(b)) and Figure (2.5(a)).
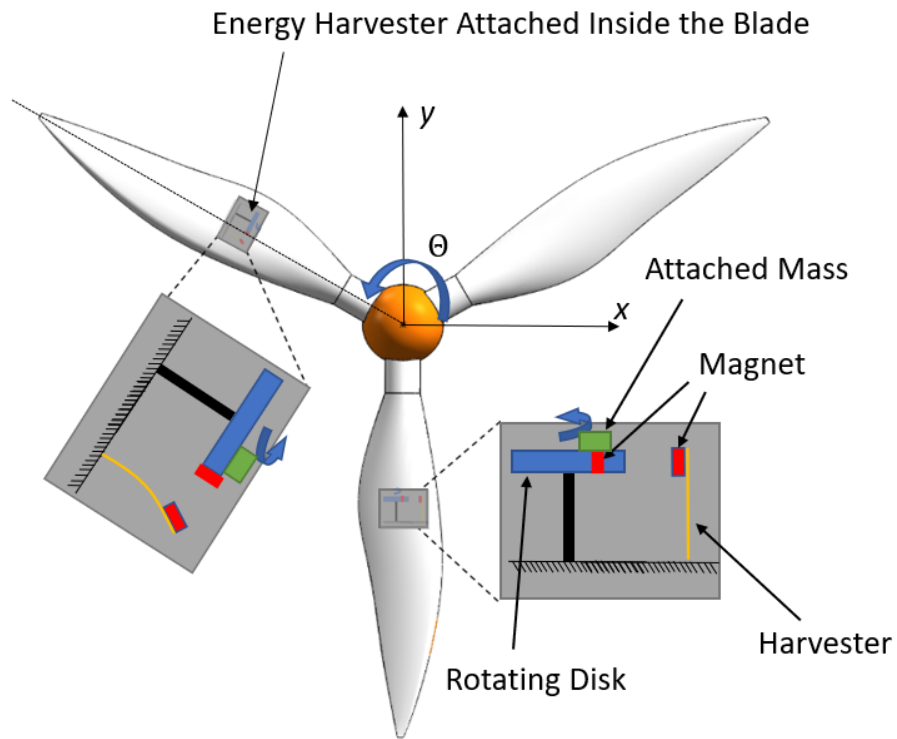
Figure (2.3) Configuration of harvester on a wind turbine blade

(a) With respect to global coordinate (x, y) (b) With respect to local coordinate (x_1, y_1)
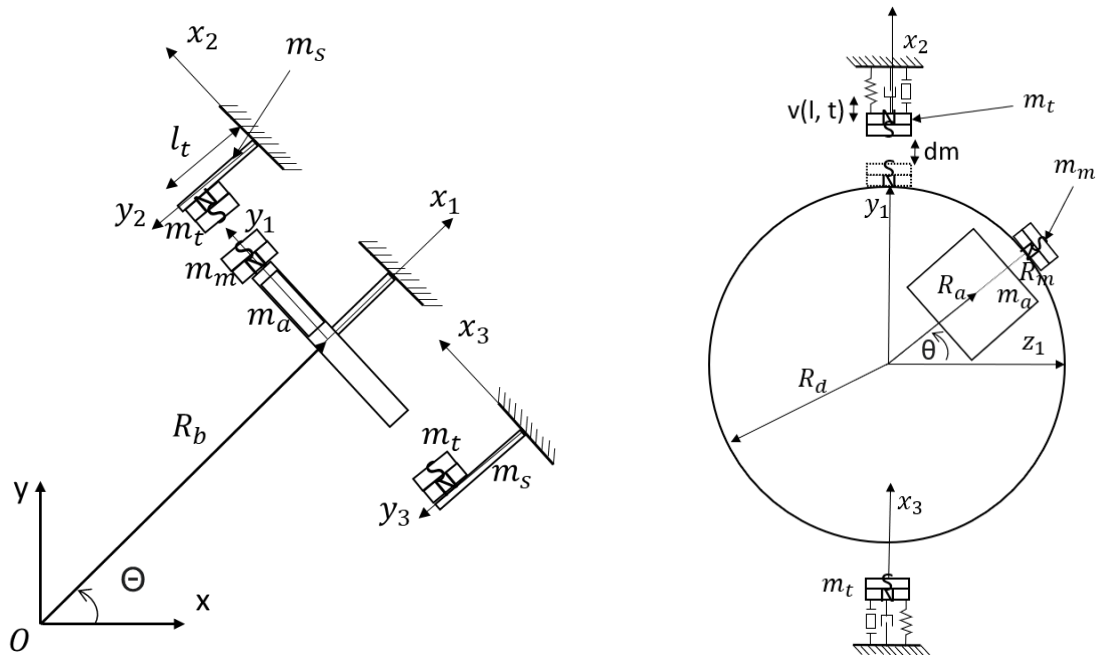
Figure (2.4) Schematic of first model of harvester setup
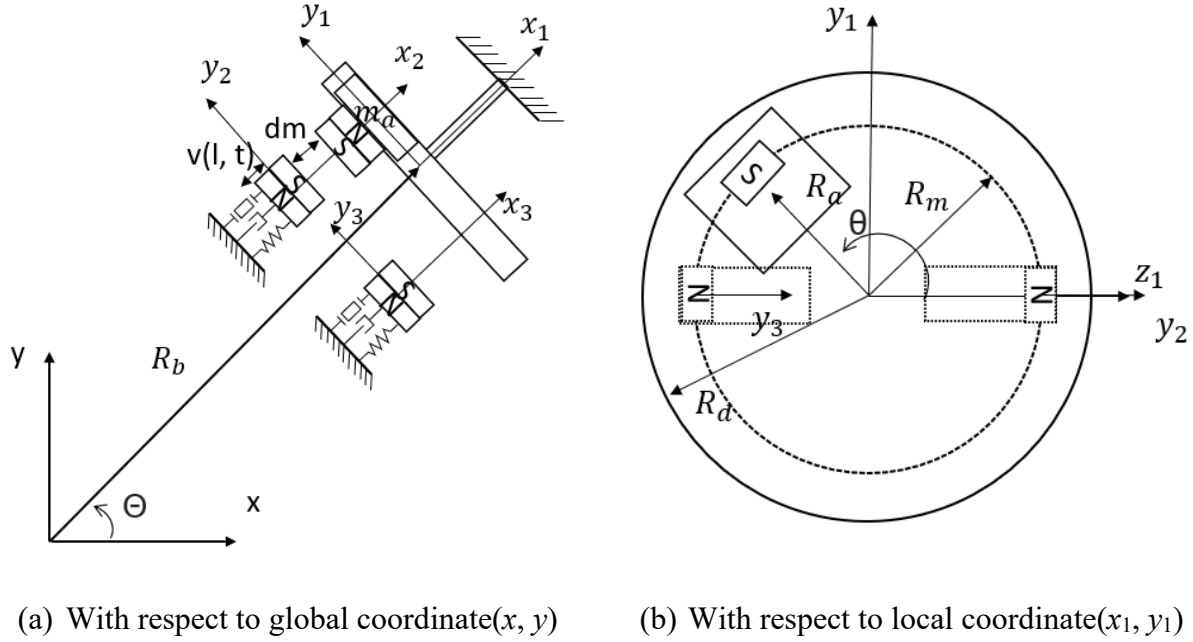
(a) With respect to global coordinate(x, y)   (b) With respect to local coordinate(x_1, y_1)

Figure (2.5) Schematic model of second model of harvester setup

The first layout is identical to the previous work (Nezami and Lee, 2020) with two cantilevered harvesters, and the second layout is motivated to use smaller device volume by relocating the harvesters within the disk area. To describe the dynamics of the EH, four coordinate systems are used: a global coordinate system (X, Y, Z) at the center of rotation of the blade, three local coordinate systems (x_1, y_1, z_1) at the center of rotation of the disk, (x_2, y_2, z_2) at the fixed end of the first cantilevered PEH beam and (x_3, y_3, z_3) at the fixed end of the second cantilevered PEH beam. The three local coordinate systems are fixed on the blade. Θ describes the blade orientation with respect to global coordinates (x, y, z), θ is the angular position of the attached mass and magnet (m_a and m_m) with respect to the local coordinates (x_1, y_1, z_1), and v_1 and v_2 is the directional position of the m_t and m_s in local coordinates (x_2, y_2, z_2) and (x_3, y_3, z_3) respectively. The detailed derivation of dynamic equations are done using Lagrange's method (not presented in this paper) similar to the work by Nezami and Lee (2020). This concept can be implemented with a larger

number of harvesters, but the authors learn by experience that the disk rotation is trapped by an increased number of magnets and the power is not generated efficiently.

3. Simulation Study and Design Optimization

The theoretical power output of the three types of harvester devices is found by solving the equations of motion derived based on the energy method. The equation is solved in MATLAB numerically using the built-in function ODE45. The equation solver simulates the harvester dynamics using a typical rotational speed of a large-scale wind turbine blade from 7 to 20 RPM (Duval, 2021; Energy.gov; Ramzy, 2022). Initial values for harvesters such as $\dot{\theta}, \ddot{\theta}, \dot{q}, \ddot{q}, V, \dot{V}$ are assumed to be zeros. The numerical results are simulated with a sufficient time span (50~60 sec) with the fixed time steps (0.01s). The power output is measured through a resistor that is connected to the harvester in parallel at every time step, and the root mean square (RMS) of these power outputs is calculated for comparison between different concepts. Then the design of each concept is optimized to maximize the power RMS.

3.1. Pendulum based Harvester

This section performs simulation and design optimization for the frequency up converter using the pendulum. The harvester dynamics equations are solved numerically using the MATLAB ODE45 solver to simulate three dynamic responses (pendulum angular position, harvester tip displacement, and the voltage) as shown in Figure (3.3) when $\Theta = 10$ RPM.

The RMS power measure during 10 blade rotations is used for performance evaluation. To account for varied harvester dynamics dependent on initial conditions and blade rotational speed, the six different initial conditions on the pendulum's angular position are simulated ($\theta = 27°$,

15°, 3°, -3°, -15°, -27°) at varied blade speed (7 and 20 at 1 RPM increment), and their average

RMS power is calculated.

The initial parameters of magnet distance, tip mass, and length of pendulum before optimization

are $d_m = 20mm, m_a = 70g, and\ r_P = 15cm$, respectively. This setup produces a power output

of 2.202mW. The maximum tip displacement is 14.7mm, which is within the constraint of

15.5mm by the manufacturer (PPA-2011, Mide Corp.). The power profile curve in Figure (3.1)

shows an increasing trend as the RPM of the blade increases (red star marks – before

optimization). However, there are significant power drops found in some RPM conditions.
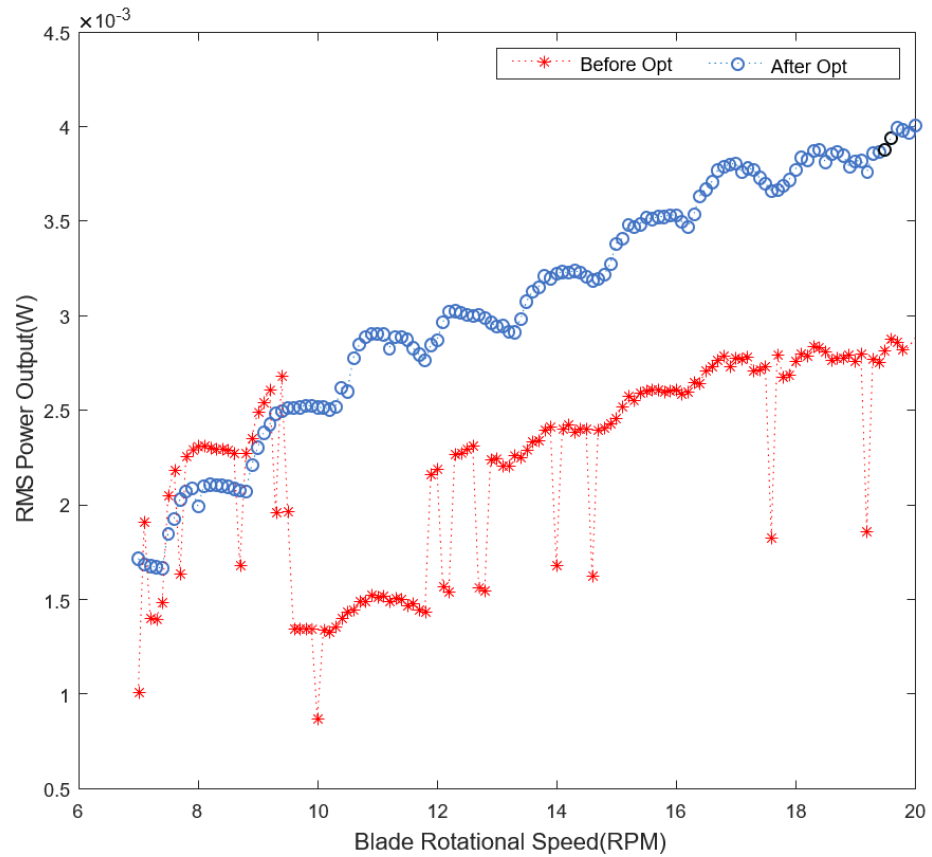
Figure (3.1) Pendulum harvester simulation result before and after optimization

The power drop issue is investigated in Figure (3.2) that shows the dynamic response of the pendulum displacement and voltage output at 10 RPM. The figure shows that the pendulum only swings on one side (negative angular position) of the circular sector, causing low voltage output from the PEH beam. This limited swing motion is due to the strong magnetic force between the pendulum and the intermediate magnets (m_p and m_m), and insufficient kinetic energy of the dropping pendulum to pass by the intermediate magnet. An increased magnetic distance or increased mass weight will solve this issue, and this investigation motivates a systematic design optimization.

(a) Pendulum displacement

(b) Voltage output
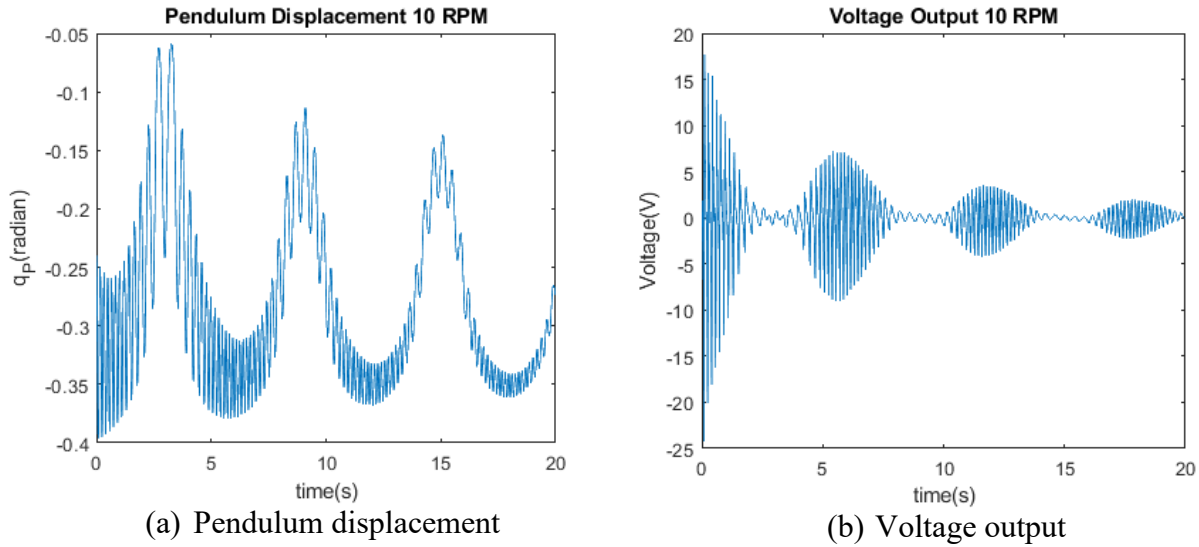
Figure (3.2) Simulated response at 10 RPM (initial condition of $\theta_0 = -15°$)

The optimization process for the pendulum harvester considers the maximization of power density using the three parameters of r_P, m_a and d_m, or:

$$max \frac{Power(r_P, m_a, d_m)}{r_P}$$

$$s.t. \quad MaxTip(r_P, m_a, d_m) < 15.5mm \qquad\qquad (3.1)$$

$$Power(r_P, m_a, d_m) > 1\ mW$$

The objective function accounts for the power per device volume, but the formulation is simplified as the power per device radius while we fix device angle (60°) and depth (80mm). Two constraints indicate to: (1) limit the maximum tip displacement for device durability; and (2) meet the minimum required power by a sensor node.

The optimization is performed using fmincon in MATLAB. The optimized result shows an overall increase in power output (blue circle marks – after optimization, Figure (3.1)) compared to the result before optimization. An overall increasing trend is demonstrated, while the power drop points are removed due to the increased inertia effect (increased mass). The power output density is increased from 0.0147W/m to 0.0338W/m and the absolute power value is increased from 2.202mW to 3.065mW. The optimized parameters are shown in **Error! Reference source not found.**) and the power improvement is enabled by reduced magnet distance (from 20mm to 17.1mm), an increase in attached mass weight (from 70g to 114.5g), and reduced pendulum length (from 15cm to 9.06cm).

Table (3.1) Optimized result – harvester on the pendulum

| Design parameters	Pendulum length (r_p)	9.06cm
	Harvester tip mass (m_a)	114.5g
	Magnet distance (d_m)	17.1mm
Harvester performances	Maximum tip displacement	12.4mm
	RMS power	3.065mW

3.2. Disk driven Harvester

For performance comparison purpose, this section performs design optimization for a frequency up converter with a disk as presented in Section 2.2. Same as the previous section, the harvester dynamics equations are solved numerically using the MATLAB ODE45 solver to simulate five dynamic responses (disk rotation, two harvester tip displacements, and two voltages). Figure (3.3) shows one case study when $\Theta = 10$ RPM. The initial model uses the following parameters: $r_p = 8$cm, $d_m = 12$mm. Figure (3.3 (a)) demonstrates the disk response, where the blue and red horizontal lines represent the positions of the first and second PEH, respectively. Whenever the disk passes through either PEH, the corresponding harvester displacement and voltage output are stimulated as shown in Figure (3.3 (b) and (c)). The blue and red colors indicate the response of harvester 1 and 2, respectively.
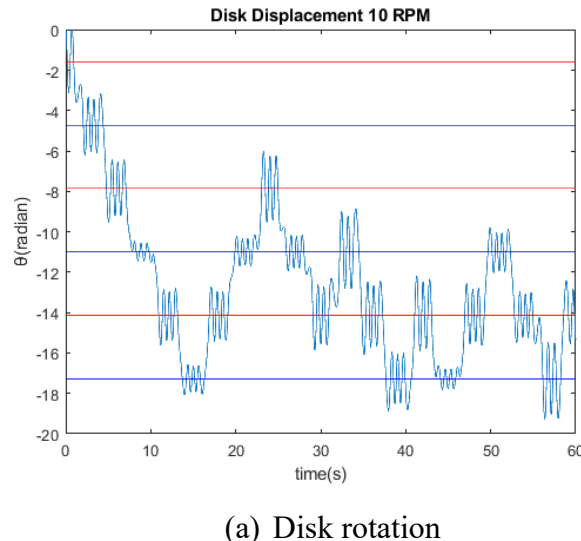
(a) Disk rotation
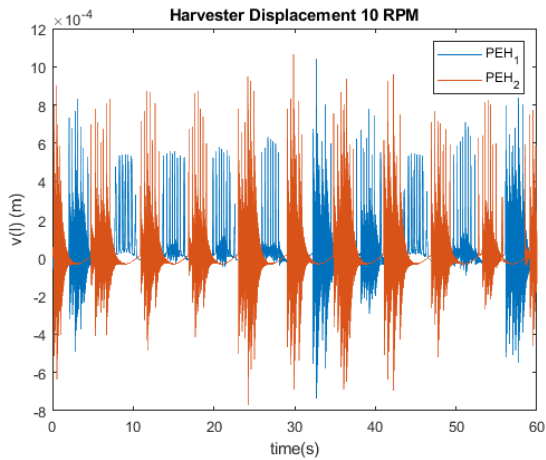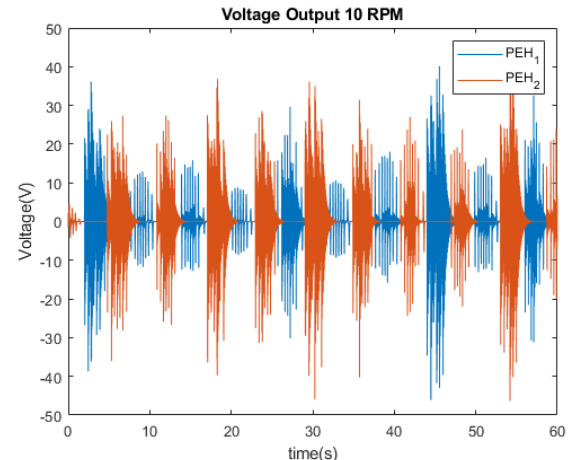
(b) Harvester displacement   (c) Voltage output

Figure (3.3) Dynamic response at 10 RPM before optimization

Figure (3.4**Error! Reference source not found.**) shows the power output of the harvester from each harvester before (star marks) and after (circle marks) optimization. Before optimization, this configuration produces 4.747mW power and 8.37 mm maximum tip displacement. While the maximum tip displacement is well below the constraint of maximum displacement of 15.5mm, it has the potential to increase power output.
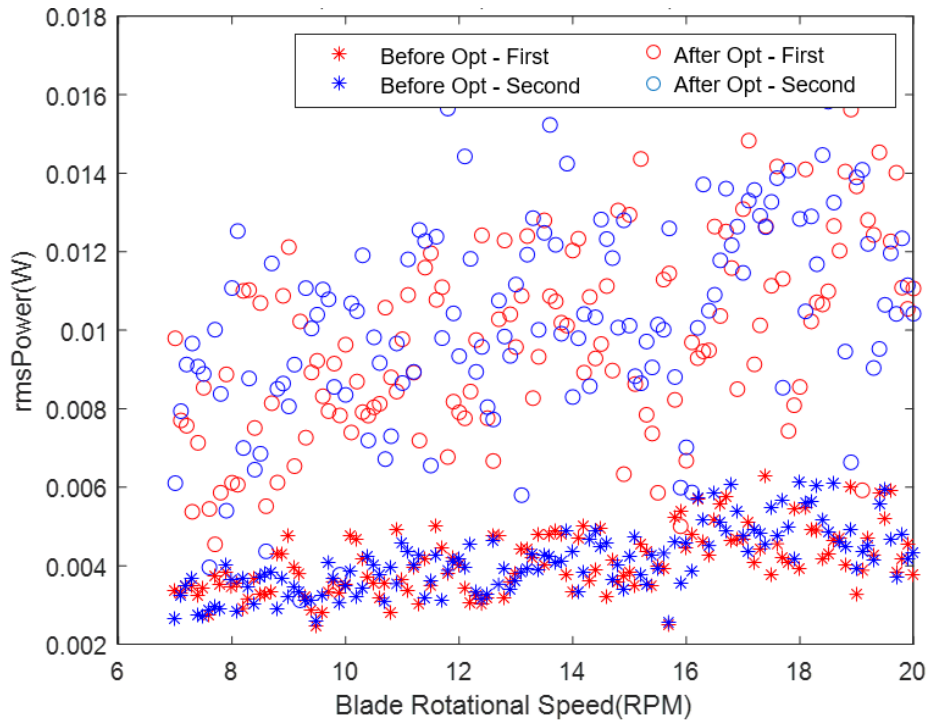
Figure (3.4) Power output density for disk concept (next to harvester) before and after optimization

A design formulation to maximize power output density is suggested as follows:

$$max \frac{Power(R_d, d_m)}{R_d}$$

$$s.t. \quad MaxTip(R_d, d_m) < 15.5mm \tag{3.2}$$

$$Power_{rms} > 2 \, mW$$

A doubled power requirement is assigned compared to the pendulum based concept, because there exist two harvesters in this concept. The optimized result is summarized shown in Table (3.2). The maximum tip displacement is found 12.605mm, less than the maximum allowed value, and the power output is obtained as 20.15mW (power sum from the two harvesters).

Table (3.2) Optimized result – harvester next to the disk

Design parameters	Disk Radius (R_d)	13.02cm
	Magnet Distance (d_m)	8.5mm
Harvester performances	Maximum tip displacement	12.605mm
	RMS power	20.15mW

A similar optimization process is run with a new setup in which the two harvesters and coupled magnets are placed on the top side of the rotating disk. Figure (3.5) shows the dynamic response before optimization, which has the same parameter as the previous disk driven harvester. By comparing these two sets of figures, Figure (3.3) and Figure (3.5), it is found that the dynamic response is less active in terms of the amplitude of disk rotation, harvester displacement, and the voltage. As the magnet and harvester sets have moved closer to the center of the disk, under the same disk rotational speed, the passing speed will be reduced, and the PEH will be stimulated by a smaller force. As a result, it is expected that this concept (harvester below the disk) produces lower power output compared to the previous concept (harvester next to the disk).
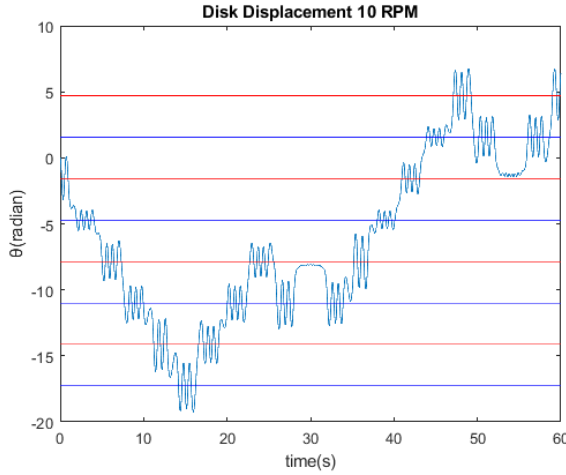
(a) Disk response
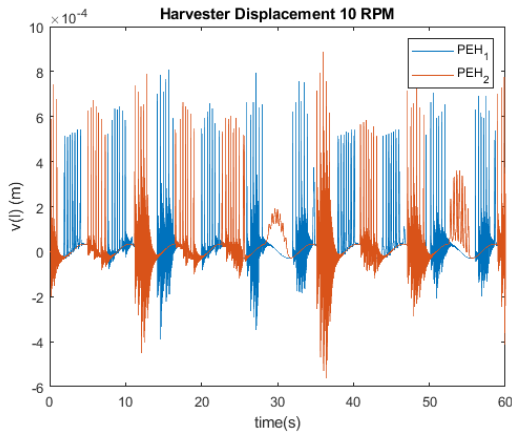
(b) Harvester displacement
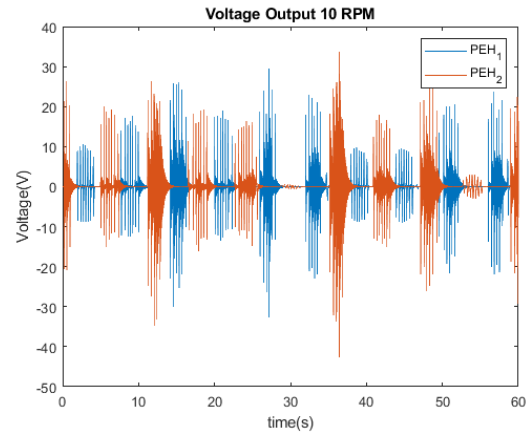
(c) Voltage output

Figure (3.5) Dynamic at 10 RPM before optimization

The power output before the optimization is 1.009mW with a maximum tip displacement of 6.421mm which is well below the constraint of 15.5mm. The same optimization process in Equation (3.2) is performed to maximize power density by changing the parameters of disk radius R_d and magnet distance d_m. In the optimized model, the maximum tip displacement is 12.64mm and the RMS power measure is obtained as 21.06mW.

Table (3.3) Optimized result – harvester below the disk

Design parameters	Disk Radius	17.72cm
	Magnet Distance	7.9mm
Harvester performances	Maximum tip displacement	12.64mm
	RMS power	21.06mW
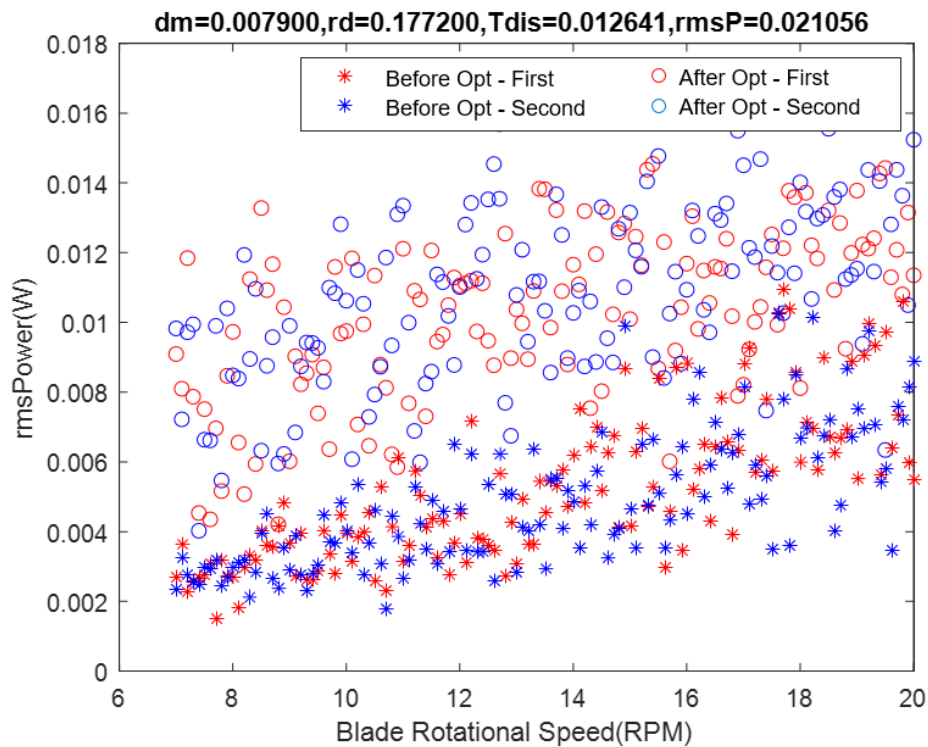
Figure (3.6) Power output density for disk concept (above harvester) before and after optimization

3.3. Simulated Result Comparison

The performance analysis of the two frequency up converters mainly focuses on the power output density of each design simulated from 7 to 20 RPM. The power densities are calculated by dividing power by length dimension (e.g., pendulum length or disk radius). As the pendulum

concept only swings a section of a circle (60°), for fairness, the power density of the pendulum obtained from Section 3.4 will be multiplied by 6 to compare with the two disk concepts that considers the power from two harvesters. The power densities of the three concepts are summarized in Table (3.4) below.

Table (3.4) Power Density Comparison

	Pendulum PEH	Disk Next to PEHs	Disk above PEHs
Power Density(W/m)	0.2030	0.1548	0.1189

The concept with the pendulum shows the highest power output density, while the disk concept (disk above harvester) produces the lowest power output density. As discussed in Section 3.2, the harvesters are moved below the disk to improve the power density, but this relocation results in slower stimulation on the PEHs and lower power generation. Overall, the pendulum based concept demonstrates efficient power generation in a limited device volume.

In the disk driven concepts, the rotation dynamics is not perfectly periodic with uncertainty that causes uneven stimulation of the harvester. However, in the pendulum based concept, each cycle of harvester vibration is identical as shown in Figure (3.21). The stable and regularized dynamic response is beneficial for electrical power charging to increase the charging efficiency (Jung et al, 2019). To conclude, the pendulum concept outperforms in terms of the power density and signal regularization.

(a) Pendulum based harvester   (b) Disk driven harvester
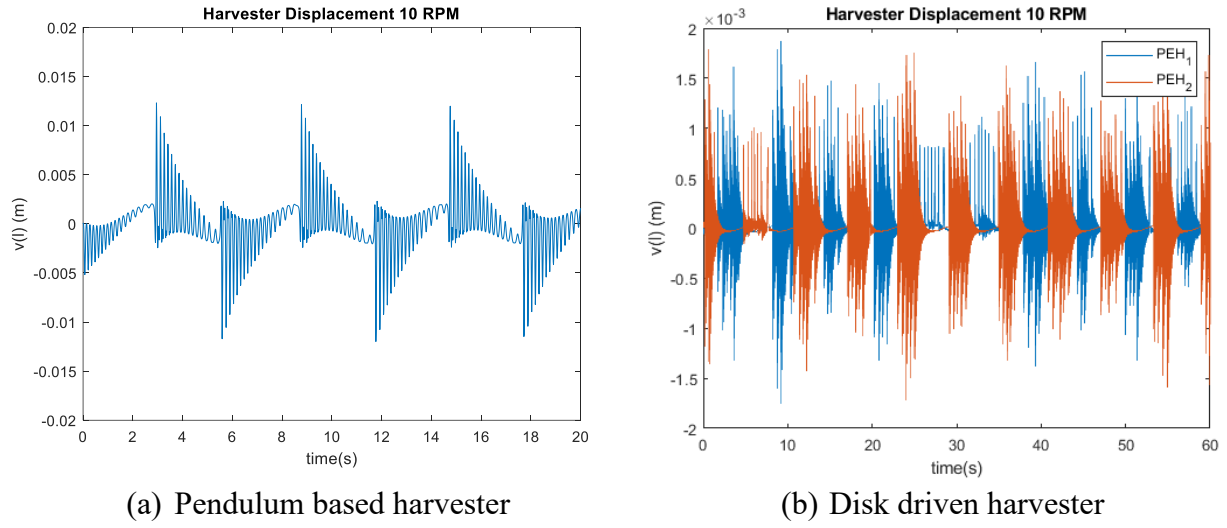
Figure (3.7) Harvester displacement responses

4. Experimental Verification

The optimized result of the pendulum based harvester will be experimentally verified in this section.

4.1. Experimental Setup

Most parts of the prototype of the pendulum harvester are created using 3D printing techniques and a Solidworks computer-aided design (CAD) model shown in Figure (4.1). This concept is designed to have various test results with changeable parameters: discrete multiple holes for adjusting the pendulum's swinging area, and the bars with the slots for continuously changeable magnetic distance. The CAD model is fabricated using the 3D printer (Gmax 1.5XT) with PLA material.
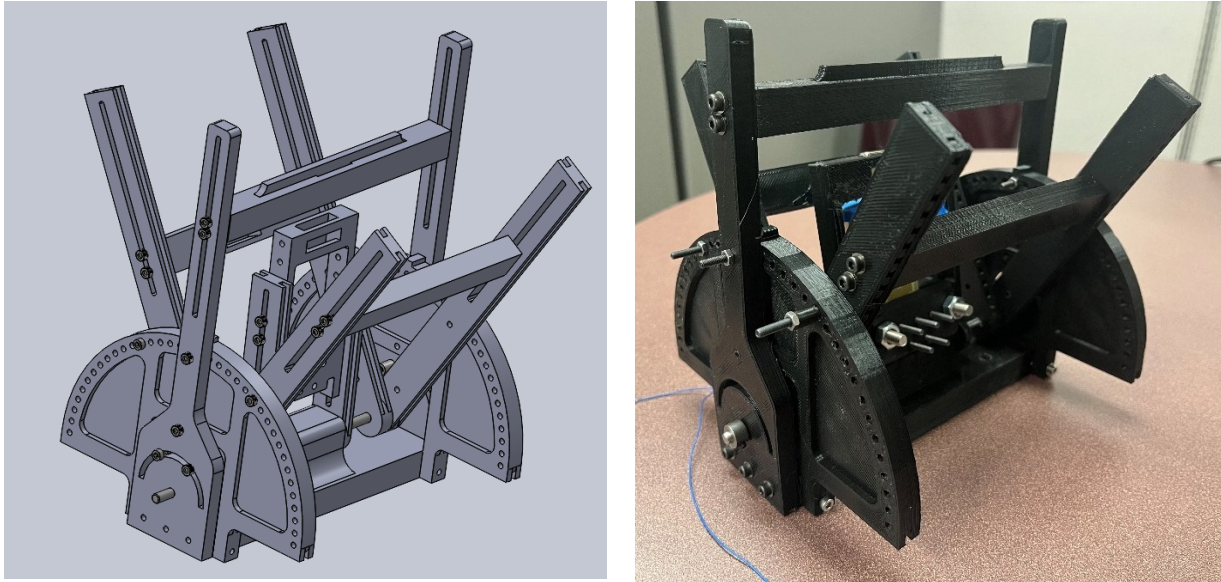
Figure (4.1) Pendulum harvester CAD model

The experimental setup is built as shown in Figure (4.2). In Figure (4.2 (a)), a wooden blade is attached to a fixture rotated by an electromotor (Marathon electric K258) to simulate the rotation of a wind turbine blade. The angular velocity of the electromotor is controlled by a variable frequency driver (Automation Direct GS2). A digital magnetic tachometer sensor is used to measure the rotational velocity of the blade. Figure (4.2 (b)) is the detailed view of the harvester device placed at the end of the wooden blade.

The prototype is attached 0.6m away from the center of the wooden blade. Four identical magnets (BX048, K&J Magnetics) are used in the prototype. The pendulum is attached to the center axis (aluminum rod) with two bearings. The PZT-5J piezoelectric beam (PPA-2011, Mide Corp.) is clamped to the pendulum with screws. The tip mass is implemented by wrapping 120g of heavy-duty lead tape. The wires from the piezoelectric beam attached along the blade pass through a slip ring to a variable resistor (Tenma 72-7270). The resistance value (51.5kΩ) is found from a sweep test on resistance, to produce the maximum power output by attaching the piezoelectric beam to the vibrator ET-126-1 (Labworks Inc.) vibrating at resonance frequency.

The oscilloscope (Rigol DS1054) is used to read voltage output from the harvester. The connection of devices is shown in Figure (4.3).

(a)Blade simulation setup
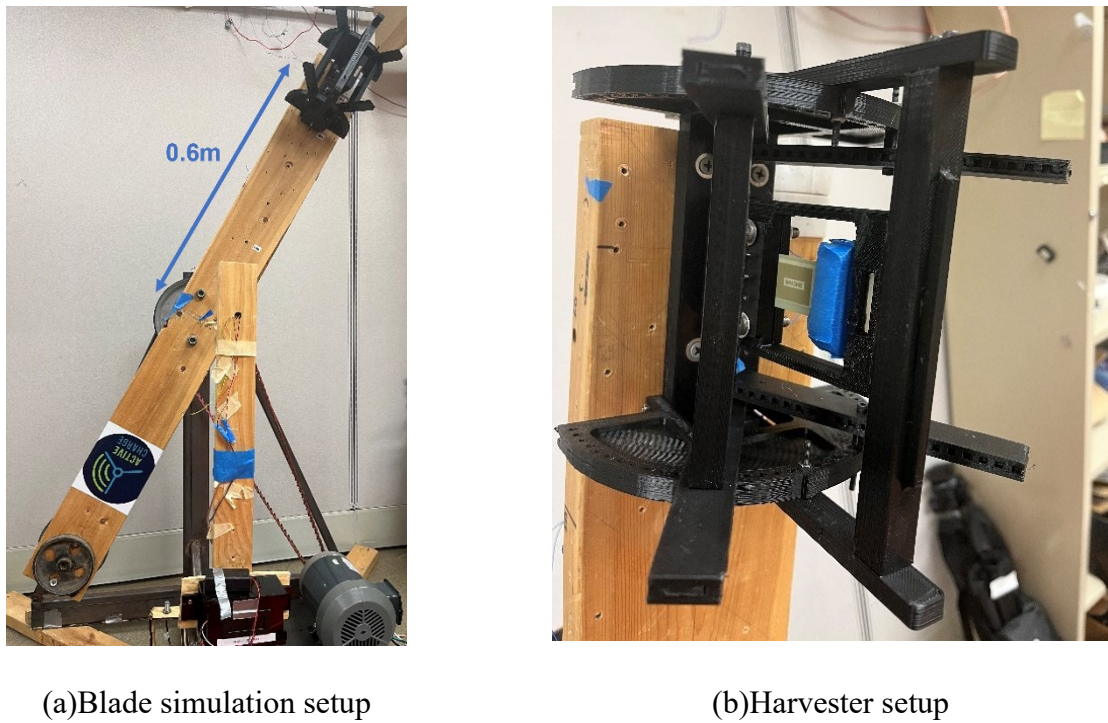
(b)Harvester setup

Figure (4.2) Experimental setup of the harvester
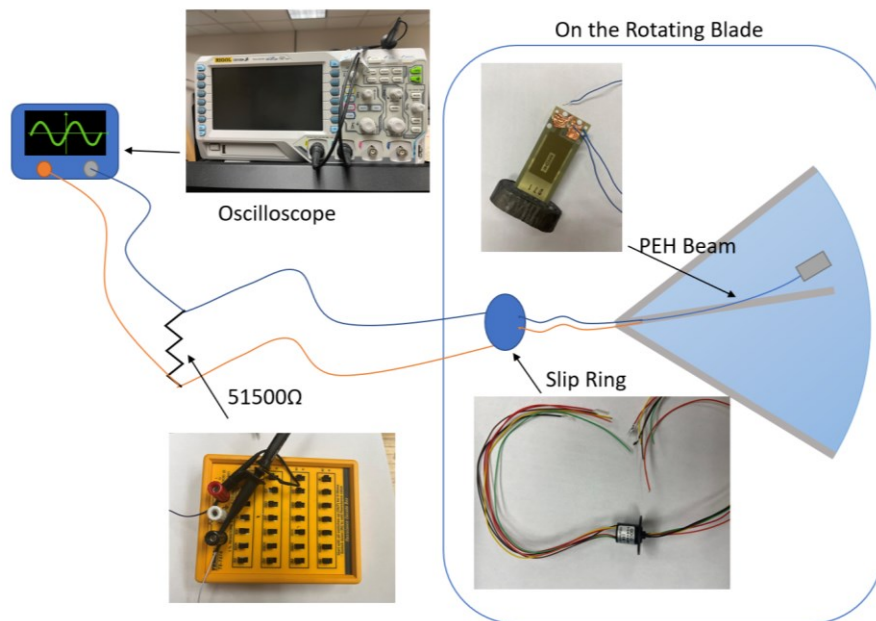
Figure (4.3) Experimental setup connection

4.2. Data Collection and Verification

To collect precise and accurate data, the experiment is run with 10 trials. Each trial collects 20 seconds of voltage output from 7 to 20 RPM of the wooden blade rotation. The sampling rate is set as 250 per second to collect the voltage history.

From multiple testing, it is found that the power output is very sensitive around the optimized magnet distance because the optimized magnet distance sits at the border of passing and bouncing behaviors. The change of the power by the magnetic distance (d_m) is displayed in Figure (4.4). A small decrease of d_m will result in drastic power decrease because the increased magnetic force, and the pendulum does not pass the intermediate magnet anymore (and bounces). A small increase of d_m (or magnetic force reduction) can stabilize the power generation performance even though the power output reduces by a smaller amount. Additionally, 3D printed structures have higher dimension deviation compared to other manufacturing techniques (Faktur, 2019), which may result in uncertain d_m parameter. For robustness, the magnetic distance is set slightly larger than what is found in the optimization study, from 17.1mm to 19 mm. The experimental result and simulated response with extended magnetic distance are shown in (Figure (4.5)).
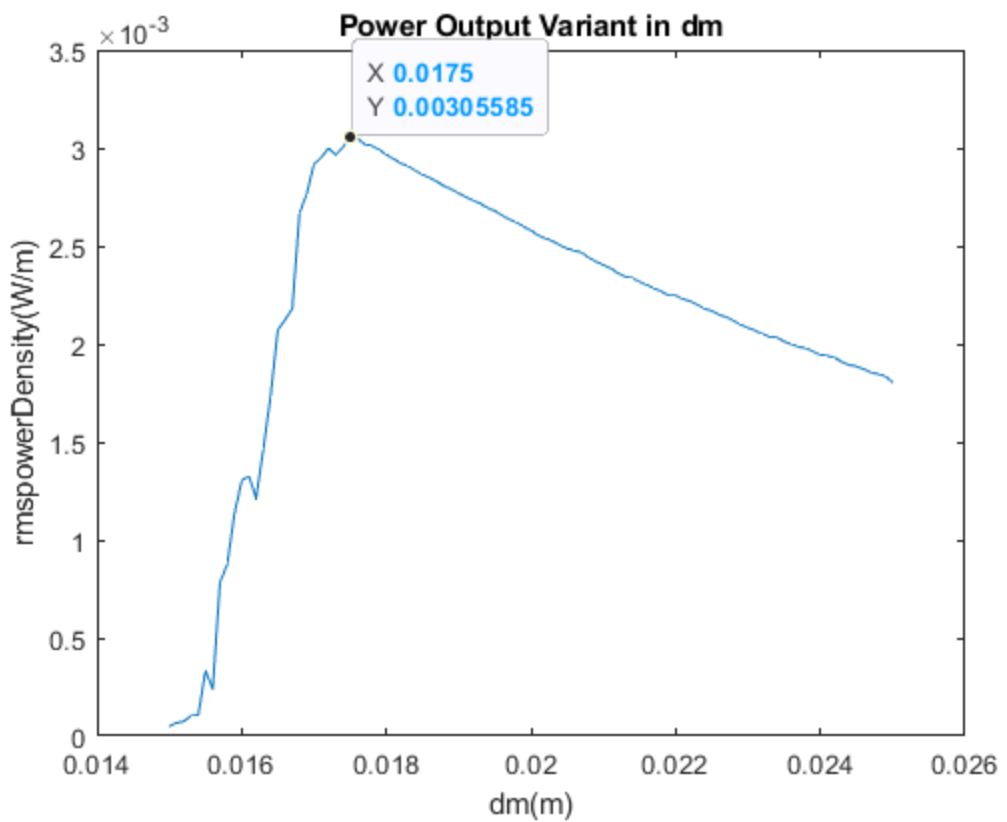
Figure (4.4): Power output vs. magnet distance
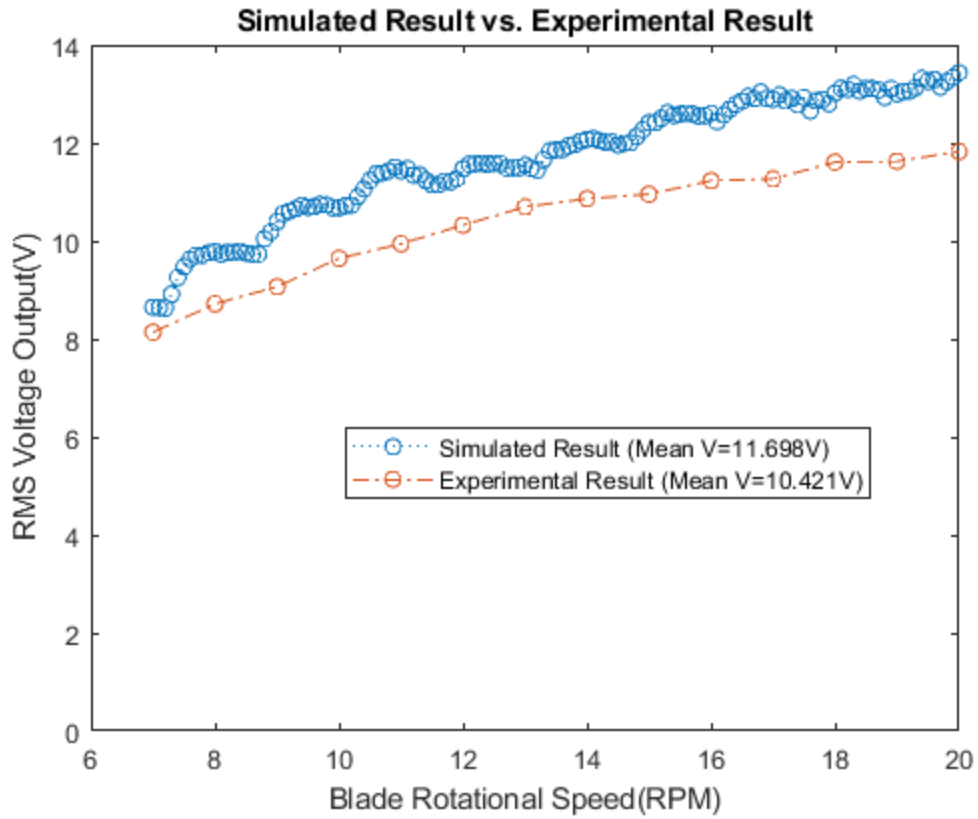
Figure (4.5) Simulated result vs. experimental result

The experimental result is found lower in mean terms of the RMS power (Figure (4.5)) and the voltage output (Figure (4.6)) compared to the simulated result. There are several possible factors to result in disagreement. Firstly, there might be inconsistent product data compared to the actual performance of the PEH beam. Secondly, the clamped boundary condition is not ideally presented due to flexibility and dimension variability of a 3D printed structure with PLA material. However, the experimental result is only 10.9% lower in mean voltage output compared to the simulated result, and the overall waveforms show good agreement.
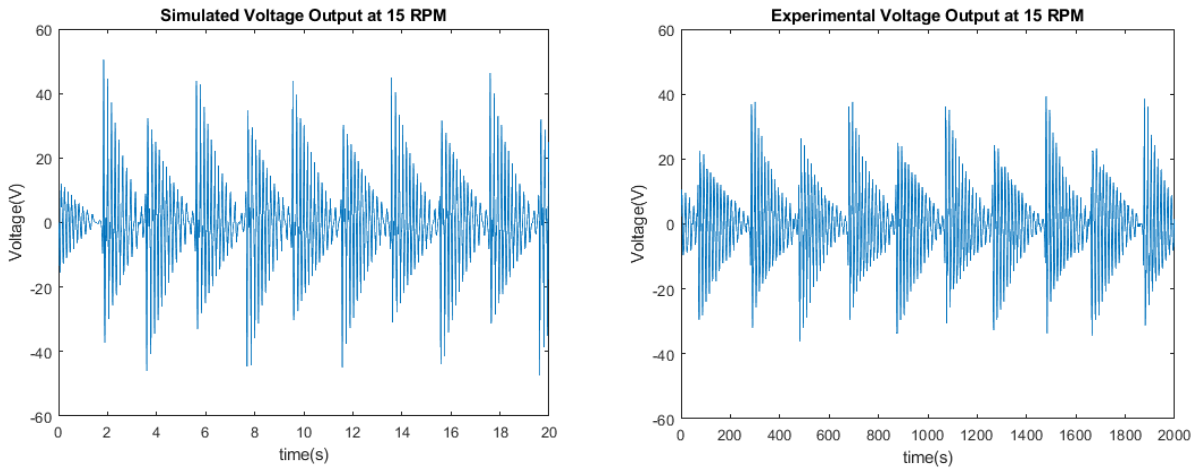
Figure (4.6) Simulated and experimental voltage output at 15 RPM blade speed

5. Conclusion

This paper introduces three concepts of piezoelectric energy harvester that is capable of collecting energy from wind turbine blade rotations. The frequency-up conversion technique is used in the three concepts to transform low rotation frequency from a wind turbine blade to the higher vibrational frequency of the PEH cantilevered beam. The mathematical models of three concepts are developed, and the dynamic responses of the harvester are simulated. Each concept is optimized with various parameters including mass, magnetic distance, size and PEH location(s), and their optimized results of each concept are compared. The pendulum based concept utilizes a pendulum that swings within a circular section confined by a pair of magnets on the outer section. A PEH beam is mounted to the pendulum, and the voltage is induced as the pendulum swings. Another magnet is intermediately placed to improve the pendulum dynamics and generate more power. The disk driven concepts, on the other hand, utilize the swinging motion of a disk to stimulate vibration on a piezoelectric beam by magnetic repelling force. Compared to the disk driven concept, the pendulum based concept produces a higher power density. The optimized result of the pendulum based concept is prototyped and tested on a

rotating structure to verify the performance experimentally. A power charging circuit needs to be designed for system integration with a monitoring sensor and a wireless transmitter for effective wind turbine blade monitoring. as future work.

6. Acknowledgements

7. Appendix – measurement of magnetic force and damping ratios

The magnetic force and the damping ratios (pendulum, PEH) need to be measured for the simulation study. The magnetic force between two magnets (BX048, K&J Magnetics) is measured experimentally using a testing instrument (Instron Electropuls E1000). The magnetic forces are measured in two different orientations Figure (7.1): pole-to-pole and side-to-side. Pole-to-pole orientation is used between pendulum magnet and intermediate magnet, and side-to-side orientation are used for the others. For the disk-driven harvester, only pole-to-pole is used.
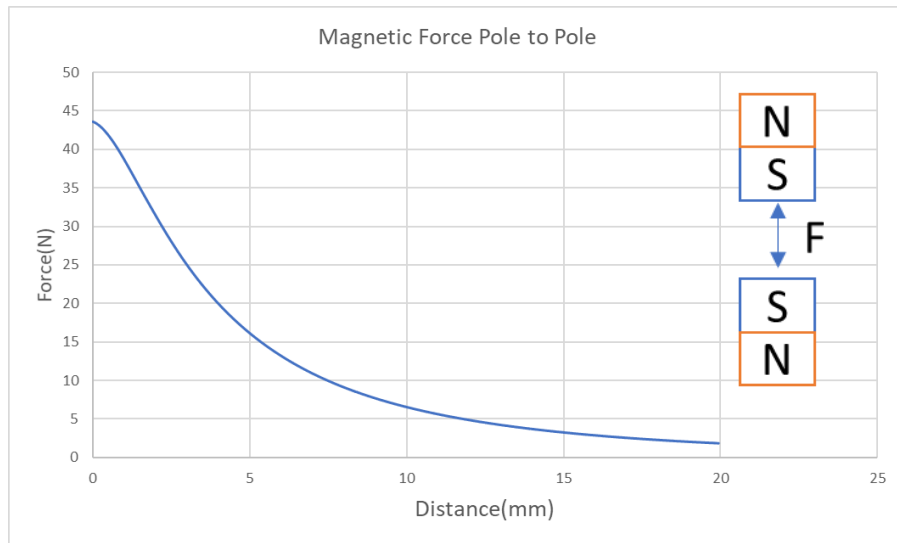
(a) Pole-to-Pole Magnetic Force
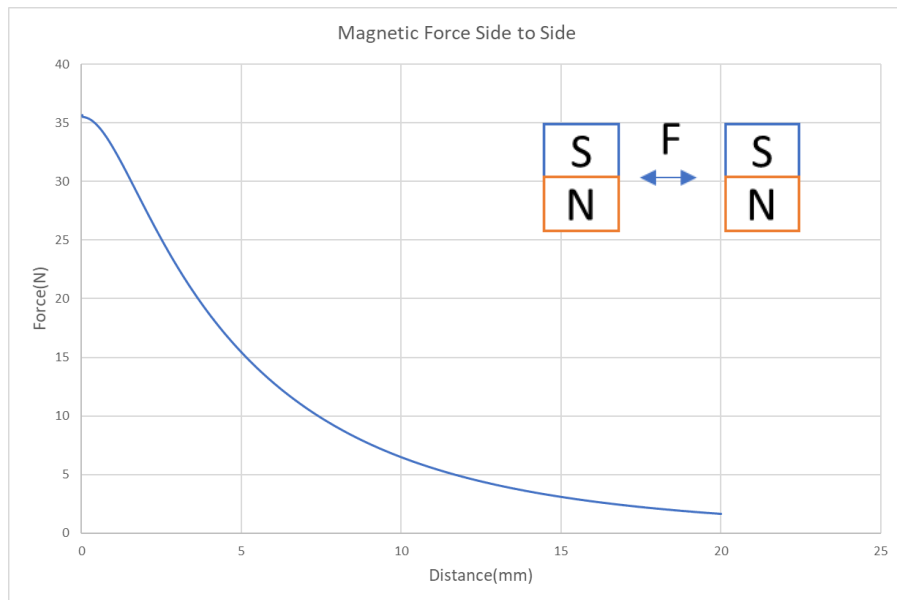
(b) Side-to-Side Magnetic Force

Figure (7.1) Experimental data for magnetic force

The experimental data is then interpolated using a two-term exponential equation or as shown in equation (3.1).

$$F(x) = ae^{bx} + ce^{dx}$$

Pole-to-Pole: $\begin{cases} a = 43.841, b = -246.66 \\ c = 4.6275, d = -52.034 \end{cases}$ (3.1)

Side-to-Side: $\begin{cases} a = 38.834, b = -195.11 \\ c = 0.93925, \ d = 1.3922 \end{cases}$

The damping ratios for the pendulum and harvester are tested using the method of logarithmic decrement. The dynamic responses of free vibration for the pendulum are recorded using a portable high-speed camera (GoPro), and the amplitudes of each cycle are measured using the video analysis software Kinovea (Kinovea, 2022) The damping ratio of the harvester beam is measured using the open circuit voltage response of free vibration for the harvester captured using an oscilloscope (Rigol DS1054), assuming its linearity to the tip vibration of the harvester. The damping ratios of the pendulum and the harvester are measured as 0.018 and 0.021, respectively. For the disk concepts, the same damping coefficient (=0.0533) from the previous study is used (Nezami and Lee, 2020).

8. Reference

Anon, How a wind turbine works - text version. *Energy.gov*. Available at:
https://www.energy.gov/eere/wind/how-wind-turbine-works-text-version [Accessed September 22, 2022].

Choudhry, I., Khalid, H.R. & Lee, H.-K., 2020. Flexible piezoelectric transducers for energy harvesting and sensing from human kinematics. *ACS Applied Electronic Materials*, 2(10), pp.3346–3357.

Duval, G., 2021. How fast do wind turbines spin? *Semprius*. Available at:
https://www.semprius.com/how-fast-do-wind-turbines-spin/ [Accessed September 22, 2022].

Erturk, A. & Inman, D.J., 2008. A distributed parameter electromechanical model for Cantilevered Piezoelectric Energy Harvesters. *Journal of Vibration and Acoustics*, 130(4).

Erturk, A. & Inman, D.J., 2011. *Piezoelectric Energy Harvesting*, Chichester: John Wiley & Sons.

Erturk, A., Renno, J.M. & Inman, D.J., 2008. Modeling of piezoelectric energy harvesting from an L-shaped beam-mass structure with an application to uavs. *Journal of Intelligent Material Systems and Structures*, 20(5), pp.529–544.

Fang, S. et al., 2019. A music-box-like extended rotational plucking energy harvester with multiple piezoelectric cantilevers. *Applied Physics Letters*, 114(23), p.233902.

Fang, S. et al., 2022. Broadband Energy Harvester for low-frequency rotations utilizing centrifugal softening piezoelectric beam array. *Energy*, 241, p.122833.

Hu, Y., Hu, H. & Yang, J., 2006. A low frequency piezoelectric power harvester using a spiral-shaped bimorph. *Science in China Series G: Physics, Mechanics and Astronomy*, 49(6), pp.649–659.

Jung, H. J., Nezami, S. and Lee, S., 2019. Power supply switch circuit for intermittent energy harvesting. Electronics, 8(12), p.1446.

Kim, H.S., Kim, J.-H. & Kim, J., 2011. A review of piezoelectric energy harvesting based on vibration. *International Journal of Precision Engineering and Manufacturing*, 12(6), pp.1129–1141.

Kinovea, 2021. A Microscope for Your Videos. Available at: https://www.kinovea.org/ [Accessed October 22, 2021].

Knight, C., Davidson, J. & Behrens, S., 2008. Energy Options for wireless sensor nodes. *Sensors*, 8(12), pp.8037–8066.

Konstantinidis, E.I. & Botsaris, P.N., 2016. Wind turbines: Current status, Obstacles, trends and technologies. *IOP Conference Series: Materials Science and Engineering*, 161, p.012079.

Liu, X., An electromagnetic energy harvester for powering consumer electronics. *TigerPrints*. Available at: https://tigerprints.clemson.edu/all_theses/1415 [Accessed September 22, 2022].

Liu, Y. et al., 2021. Piezoelectric energy harvesting for self-powered wearable upper limb applications. *Nano Select*, 2(8), pp.1459–1479.

MarkusMay, 2019. Accuracies and tolerances in 3D printing. *3Faktur*. Available at: https://3faktur.com/en/accuracies-and-tolerances-in-3d-printing/#:~:text=In%20most%20additive%20technologies%2C%20the,injection%20molding%20or%20CNC%20machining. [Accessed September 22, 2022].

Nezami, S. & Lee, S., 2020. Nonlinear Dynamics of a rotary energy harvester with a double frequency up-conversion mechanism. *Journal of Computational and Nonlinear Dynamics*, 15(9).

Ong, Z.C., Huang, Y.-H. & Chou, S.-L., 2019. Resonant frequency reduction of piezoelectric voltage energy harvester by elastic boundary condition. *Journal of Mechanics*, 35(6), pp.779–793.

Palazzolo, A.B., 2016. *Vibration theory and applications with finite elements*, Chichester, West Sussex, United Kingdom: John Wiley & Sons, Inc.

Park, J., Lee, S. and Kwak, B.M., 2012. Design optimization of piezoelectric energy harvester subject to tip excitation. *Journal of Mechanical Science and Technology*, 26(1), pp.137-143.

Pozzi, M. & Zhu, M., 2012. Characterization of a rotary piezoelectric energy harvester based on plucking excitation for knee-joint wearable applications. *Smart Materials and Structures*, 21(5), pp.055004.

Ramzy, 2022. How fast does a wind turbine spin? *linquip*. Available at: https://www.linquip.com/blog/how-fast-does-a-wind-turbine-spin/ [Accessed September 22, 2022].

Shaikh, F.K. & Zeadally, S., 2016. Energy harvesting in wireless sensor networks: A comprehensive review. *Renewable and Sustainable Energy Reviews*, 55, pp.1041–1054.

Su, W.-J., Zu, J. & Zhu, Y., 2013. Design and development of a broadband magnet-induced dual-cantilever piezoelectric energy harvester. *Journal of Intelligent Material Systems and Structures*, 25(4), pp.430–442.

Wang, G. et al., 2019. Nonlinear magnetic force and dynamic characteristics of a tri-stable Piezoelectric Energy Harvester. *Nonlinear Dynamics*, 97(4), pp.2371–2397.

Wiser, R. & Bolinger, M., 2019. 2018 distributed wind market report - energy. *Energy.gov*. Available at: https://www.energy.gov/sites/prod/files/2019/08/f65/2018%20Distributed%20Wind%20Market%20Report.pdf [Accessed September 23, 2022].

Wu, H. et al., 2014. Development of a broadband nonlinear two-degree-of-freedom piezoelectric energy harvester. *Journal of Intelligent Material Systems and Structures*, 25(14), pp.1875–1889.

Xing, X. et al., 2009. Wideband vibration energy harvester with high permeability magnetic material. *Applied Physics Letters*, 95(13), p.134103.

Xu, X. et al., 2018. Application of piezoelectric transducer in energy harvesting in Pavement. *International Journal of Pavement Research and Technology*, 11(4), pp.388–395.

Yan, B. et al., 2020. Scavenging vibrational energy with a novel Bistable Electromagnetic Energy Harvester. *Smart Materials and Structures*, 29(2), p.025022.

Yang, Y. et al., 2014. Rotational piezoelectric wind energy harvesting using impact-induced resonance. *Applied Physics Letters*, 105(5), p.053901.

Yang, Z. et al., 2018. High-performance piezoelectric energy harvesters and their applications. *Joule*, 2(4), pp.642–697.

Zhang, J. et al., 2017. A rotational piezoelectric energy harvester for efficient wind energy harvesting. *Sensors and Actuators A: Physical*, 262, pp.123–129.